

EFFECT OF HORIZONTAL RESOLUTION IN A FINITE-DIFFERENCE MODEL OF THE GENERAL CIRCULATION

ROBERT E. WELLCK, AKIRA KASAHARA, WARREN M. WASHINGTON, and GLORIA DE SANTO

National Center for Atmospheric Research,¹ Boulder, Colo.

ABSTRACT

The effect is studied of varying the horizontal grid resolution on the simulation of January climate in the NCAR general circulation model. The six-layer model with a 3-km thickness was used for this experiment. For a fixed vertical resolution three different versions of the model were programmed, having horizontal grid increments of 10°, 5°, and 2.5° in longitude and latitude. The model includes various physical processes operating in the atmosphere including a hydrological cycle, solar and terrestrial radiation, and boundary layers; but the dynamic effect of orography was suppressed.

Results from the three runs with different horizontal resolution were compared by computing various zonally averaged meteorological variables including mean and eddy meridional fluxes of momentum, heat, and water vapor. It is shown that the zonally averaged temperature and specific humidity fields are simulated well by the three different resolution models. However, for the simulation of the wind field the 10° mesh is too coarse, whereas that of the 2.5° mesh is closer to reality. The reason for this is investigated by analysis of the mean and eddy meridional momentum transports.

The analysis of kinetic energy spectra also supports the desirability of a 2.5° mesh for the simulation of large-scale motions. A remarkable improvement in the 2.5° mesh simulation is the increase of eddy kinetic energy in the long waves of wave numbers 1 to 4.

1. INTRODUCTION

Ever since numerical weather prediction methods were first developed, one of the basic questions has been the selection of adequate finite-difference grid sizes in both the horizontal and vertical directions. Obviously, from the standpoint of the accuracy of finite-difference calculations, we desire to have the highest possible resolution, whereas from the standpoint of computational economy we desire to have the coarsest possible resolution. Since the question of the grid resolution is closely related to the scale of the phenomena concerned, we shall limit our discussion to the planetary scale and synoptic scale motions of the atmosphere.

The purpose of this paper is to report our comparative study of the effect of varying the horizontal grid resolution on simulation of the general circulation patterns using the six-layer version of the National Center for Atmospheric Research (NCAR) general circulation model (GCM). With a 3-km layer thickness, the model atmosphere extends up to 18 km in height. For this fixed vertical resolution we programmed three different versions with horizontal grid increments of 10°, 5°, and 2.5° in longitude and latitude. These represent NCAR's 5° resolution model, a coarser resolution model of 10°, and a finer resolution model of 2.5°. The 2.5° model also represents the limit of NCAR's present in computer capability terms of both storage capacity and computational speed. We present results from time integrations with the three

different horizontal grid resolutions which simulate January climate starting from identical initial conditions.

In section 2, we give a brief description of the three versions of the GCM and the initial conditions used. In section 3, we present the zonally averaged values of some representative meteorological variables and compare them with observed long-term mean distributions. In section 4, we perform an analysis of the eddy strength to show how the horizontal resolution influences the eddy transport quantities. In section 5, we analyze the spectra of eddy kinetic energy computed from the three versions and compare these with observed distributions. The conclusions are stated in section 6.

2. DESCRIPTION OF THE MODEL

Here we describe briefly the NCAR GCM, with emphasis on the grid structure and the differences among the 10°, 5°, and 2.5° versions of the model.

The NCAR GCM is global and uses spherical polar coordinates in which λ is longitude, φ is latitude, and the vertical coordinate is height, z . The prognostic variables are the longitudinal and latitudinal components of momentum, ρu and ρv , the pressure, p , and the water vapor content, ρq , where q is the specific humidity. The diagnostic variables are the vertical velocity, w , the temperature, T , and the density, ρ .

Many physical processes governing the large-scale motion of the atmosphere are considered. These include the absorption of the incoming solar energy in the atmosphere, cooling due to infrared radiation, heating due to the

¹ The National Center for Atmospheric Research (NCAR) is sponsored by the National Science Foundation.

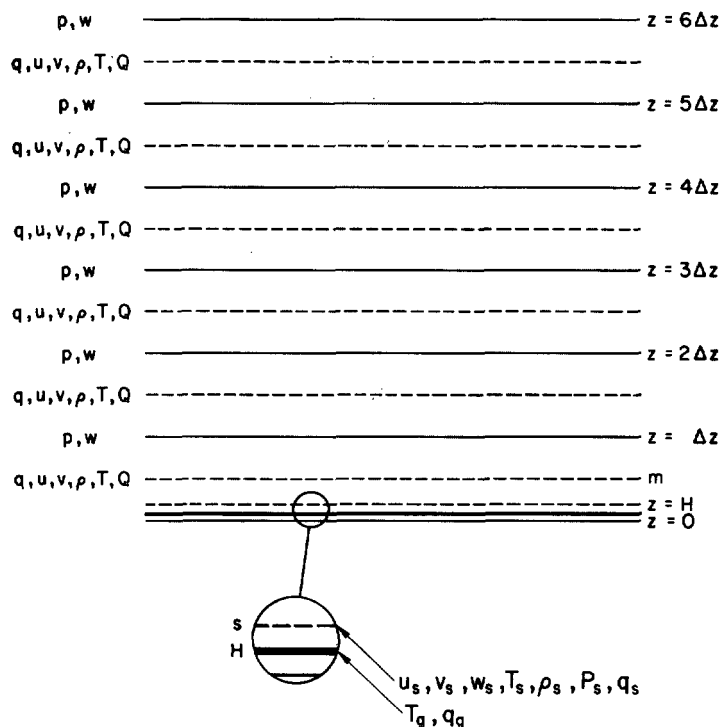


FIGURE 1.—Vertical cross-section of the six-layer NCAR general circulation model without earth's orography.

release of latent heat of water vapor condensation, effects of planetary and surface boundary layers in the transports of sensible heat and the evaporation of water vapor from the earth's surface, and dissipation of momentum by small-scale turbulence. Surface temperature over land and ice-snow regions is calculated from a heat balance equation taking into account day-night variations in the solar radiation. Details of the NCAR model may be found in Kasahara and Washington (1967, 1969) and Washington and Kasahara (1970).

Figure 1 shows the vertical grid structure consisting of six 3-km layers. The lower boundary level, s , is placed at anemometer height (approximately 10 m above the earth's surface) and the H -level represents the earth's orography. Although the dynamical effect of mountains is incorporated in the NCAR GCM, we suppressed the dynamical effect of mountains by assuming the height of mountains to be $H=10$ m in this study because mountain height data were not readily available for the 2.5° resolution model. Figure 2 shows the space-time relationship of the horizontal grid. All prognostic and diagnostic variables in a vertical column, defined at the levels shown in figure 1, are at the same time level. The spherical coordinate system poses a computational problem because the longitudinal distance between grid points approaches zero at the poles. In order to maintain a fairly constant distance between grid points for linear stability of the difference scheme, the number of grid points is reduced on the latitude circles from 60°N and 60°S to the poles. A centered or leapfrog time-difference scheme is used together with centered space differences to integrate the prognostic equations. The nonlinear viscosity formulation

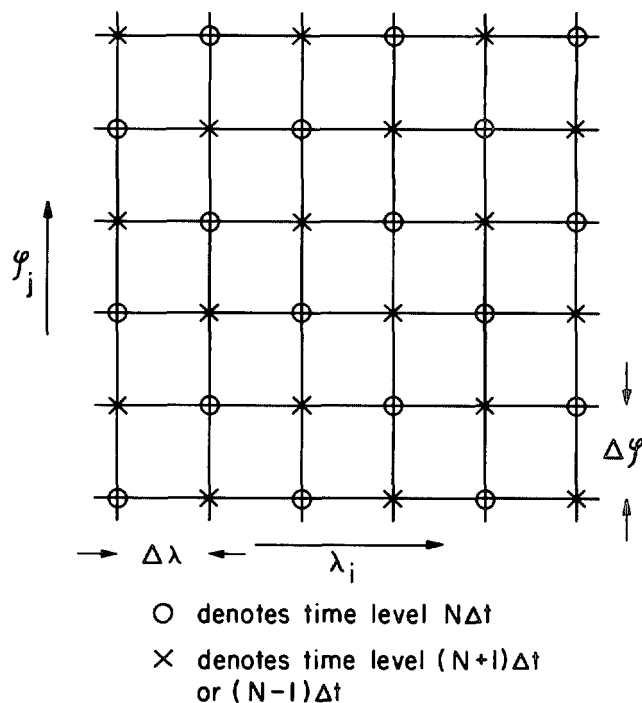


FIGURE 2.—Horizontal grid structure of the NCAR model at two time levels. $\Delta\lambda$ is the grid increment in longitude and $\Delta\phi$ in latitude. In the model calculations we assume $\Delta\lambda=\Delta\phi$.

introduced by Smagorinsky (1963) is used to obtain computational stability of the momentum and water vapor equations, and a small nonlinear smoothing is applied to the pressure on every time step. In addition, a convective adjustment is used to insure gravitational stability. For computational details see Olinger et al. (1970).

In this resolution experiment the horizontal mesh is varied, ranging between 10° , 5° , and 2.5° in longitude and latitude, as illustrated in figure 2, for the fixed vertical resolution of six 3-km layers. Figures 3, 4, and 5 show the horizontal coordinate meshes for different resolutions over a limited portion of the globe which includes the United States. The figures show the three types of regions considered: the circles designating ocean, the crosses land, and the triangles ice-snow regions. As can be seen, the 10° mesh is very coarse (there are only nine grid points covering the United States), the 5° mesh gives better definition, and the 2.5° mesh delineates the land outlines fairly well. There are 540 mesh points with 10° resolution, 2,160 with 5° resolution, and 8,640 with 2.5° resolution.

The initial conditions used for this experiment were based on an isothermal atmosphere at rest;

$$\begin{aligned} T &= 240^\circ\text{K}, \\ p(z) &= 1013 \exp[-gz/RT] \text{ mb}, \\ \rho u &= \rho v = \rho q = 0, \end{aligned}$$

where g is the acceleration due to gravity and R is the gas constant.

The following external conditions are prescribed for the simulation of January climate with the model:

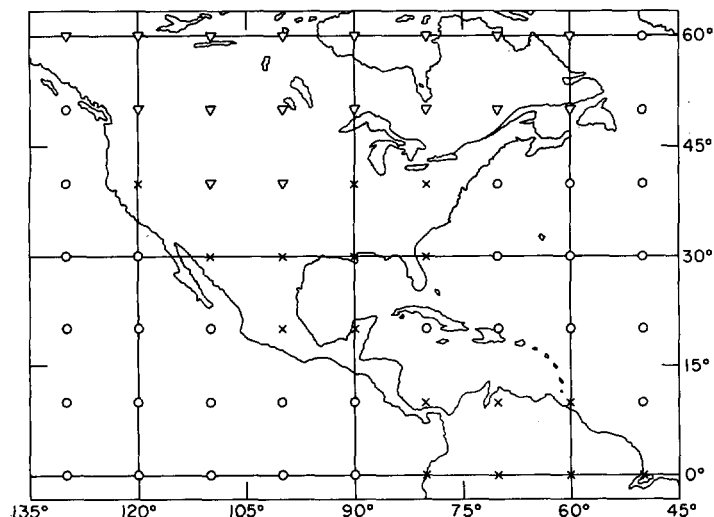


FIGURE 3.—Horizontal grid for the 10° mesh over a limited portion of the globe. Circles denote ocean, crosses denote land, and triangles denote ice-snow regions.

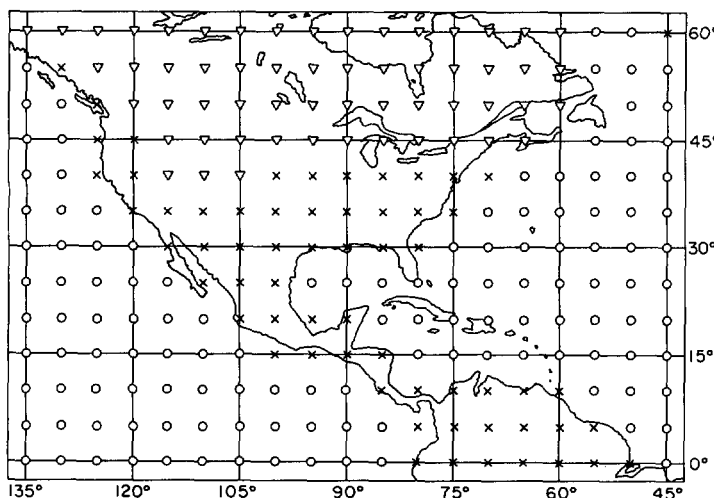


FIGURE 4.—Same as figure 3, but for the 5° mesh.

1. A monthly mean distribution of the ocean surface temperature for January. Albedo values are specified at the grid points of land and ice-snow areas.

2. Mean January zonal distributions of cloudiness at the 3- and 9-km levels for the purpose of radiation calculations.

3. The sun's declination for mid-January (-21.2°).

The time steps used for the numerical integration were 12 min, 6 min, and 3 min for the 10°, 5°, and 2.5° resolutions, respectively, to insure computational stability. We have run the 5° resolution case to day 80. Since this calculation was started from an isothermal atmosphere, large-scale monsoons developed at the onset due to heating differences between land and oceans. After about 15 days, the north-south temperature gradients become so large that the large-scale monsoonal circulation breaks down into eddy motions due to baroclinic instability. After about day 20, the flow pattern becomes meteorological and the global average of kinetic energy becomes fairly constant. We have computed zonal mean values of various meteorological

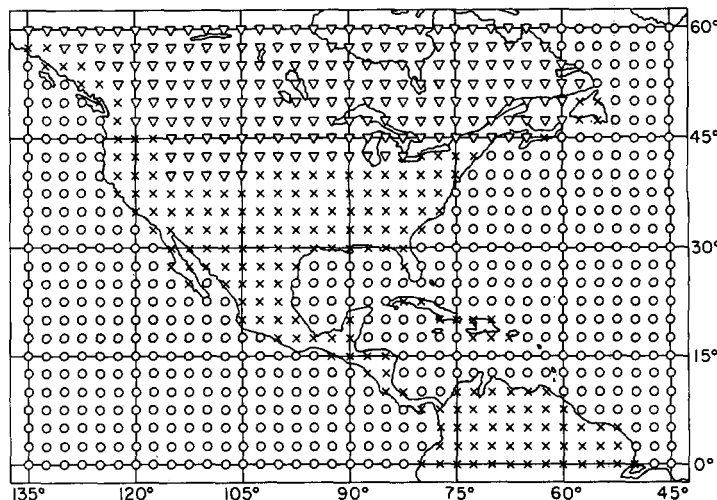


FIGURE 5.—Same as figure 3, but for the 2.5° mesh.

logical variables for the 10-day period of days 21–30 and compared them with values for the 10-day period of days 31–40. Although some variables related to the wind field show gradual changes with time, the zonal mean values for the 10-day period of days 21–30 were considered to be acceptable for the present experiment. Thus, the 2.5° case was only run to day 30. (NCAR's Control Data Corporation 6600 computer requires 8 hr to run 1 atmospheric day for the 2.5° case.) The 10° case was run to day 40, although there would have been no difficulty in running the model further.

3. ZONAL MEAN QUANTITIES

In this section we will show zonally averaged values of some representative meteorological variables that can be compared with long-term observed mean values. The zonal mean values are computed for the period of days 21–30.

Figure 6 presents the latitude-height distributions of the zonally averaged temperature field. The upper left and right pictures are for the 10° and 5° meshes and the lower left picture is for the 2.5° mesh. We see that the three meshes produced temperature distributions similar to the observed temperature distribution for January (lower right). The observed temperature distribution was constructed from data by Palmén and Newton (1969) for the Northern Hemisphere and Taljaard et al. (1969) for the Southern Hemisphere. A major discrepancy between the observed and computed distributions is the models' incapability of producing the observed colder tropical upper troposphere. This shortcoming seems to be due to the upper boundary condition that the vertical motion vanishes at the top boundary, located at 18 km. This kinematic constraint prevents adiabatic cooling in the upper troposphere, particularly in the Tropics. The upper boundary condition also failed to produce a warm Antarctic lower stratosphere in all three mesh cases. The extension of the height of the upper boundary and the incorporation of ozone heating into the NCAR GCM improve

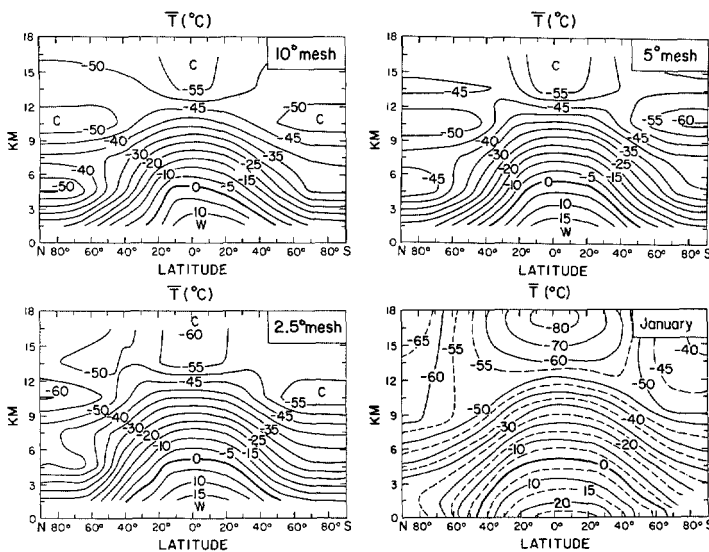


FIGURE 6.—January latitude-height distributions of zonally averaged temperature, \bar{T} , for the three mesh cases. The lower right picture shows the climatological temperature distribution.

the simulation of the lower stratospheric temperature distribution, as shown in a preliminary report by Kasahara (1970).

Figure 7 shows the latitude-height distribution of the zonally averaged specific-humidity field. As in the case of the temperature field, the three different cases produced similar distributions of zonally averaged specific humidity that agree with the observed distribution shown by the lower right picture in figure 7. The observed distribution was prepared based on data by Peixoto and Crisi (1965). The humps in the computed specific-humidity distributions in the equatorial regions are produced by the contrast in the specific-humidity values in the ascending branch and descending branches of the Hadley circulation.

Figures 6 and 7 may give the impression that the increase in the horizontal grid resolution does not make much difference in the simulation of zonally averaged variables. This is not the case, as can be seen from figure 8, which shows the distributions of the longitudinally averaged zonal wind component, \bar{u} . With the 10° mesh, the westerly jet maxima appear too far equatorward and with less intensity compared to the observed distribution shown by the lower right picture. The sources for the observed data are Palmén (1964) based on Crutcher (1961) for the Northern Hemisphere and van Loon et al. (1971) for the Southern Hemisphere.

In the 2.5° mesh model, the Northern Hemisphere westerly jet moved too far north. The reason for this is puzzling and we shall come back to the question later. However, the intensity of the Southern Hemisphere jet has improved with use of the 2.5° mesh relative to the coarser grids. We notice the tendency toward a jet core that appears to be narrower in latitudinal width in the high resolution model. The occurrence of weak tropical easterlies is not simulated satisfactorily by any of the cases.

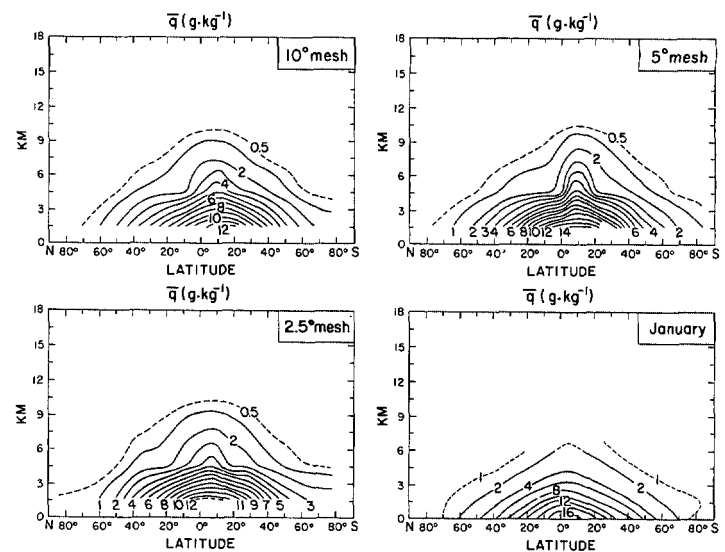


FIGURE 7.—January latitude-height distributions of zonally averaged specific humidity, \bar{q} , for the three mesh cases. The lower right picture shows the climatological specific-humidity distribution.

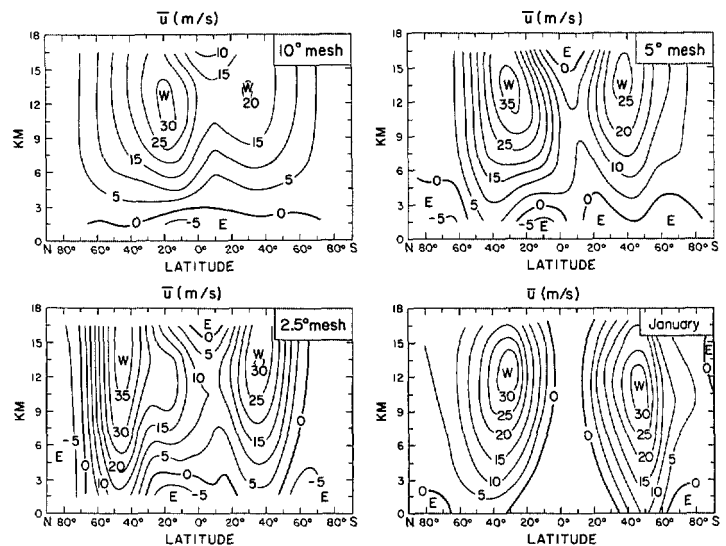


FIGURE 8.—January latitude-height distributions of zonally averaged zonal wind component, \bar{u} , for the three mesh cases. The lower right picture shows the climatological zonal wind field.

Figure 9 shows the zonally averaged distributions of the meridional wind component, \bar{v} . The lower right picture presents the observed distribution of \bar{v} for December–February after Kidson et al. (1969). The observed values appear to be quite reasonable in the Tropics, but at mid-latitudes they are too large to satisfy mass balance requirements. We did not make any attempt to adjust this data. Except for the 10° mesh which produces an unusual vertical distribution of \bar{v} in the tropical lower troposphere, both the 5° and 2.5° mesh cases yield reasonable distributions of \bar{v} .

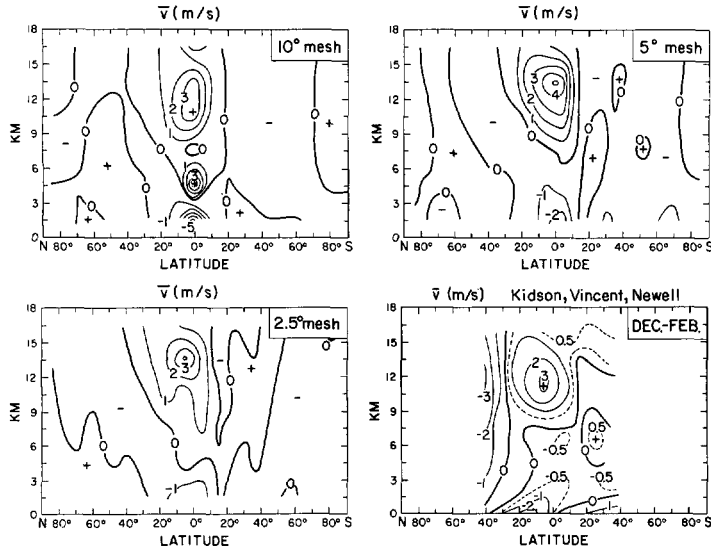


FIGURE 9.—Same as figure 8, but for the meridional wind component, v .

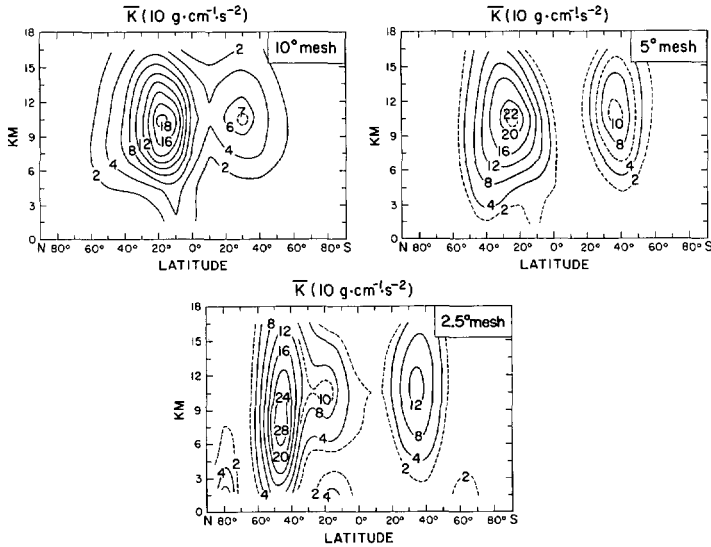


FIGURE 10.—Latitude-height distributions of the zonally averaged zonal kinetic energy defined by eq (3) for the three mesh cases.

4. MERIDIONAL TRANSPORTS BY EDDY MOTION AND MEAN CIRCULATION

The zonal mean quantities presented in the previous section illustrate some effects due to increased horizontal grid resolution upon the simulation of the global mean circulation. However, these quantities do not reveal explicitly the effects of increased horizontal grid resolution on eddy motions. Therefore, we present some meridional eddy transports computed from the three different cases and compare them with both observed data and the computed meridional transports due to the mean circulation.

Let us discuss nomenclature first. We define the zonal average, denoted by an overbar, for any variable, A , by

$$\bar{A} = \frac{1}{2\pi} \int_0^{2\pi} A d\lambda \quad (1)$$

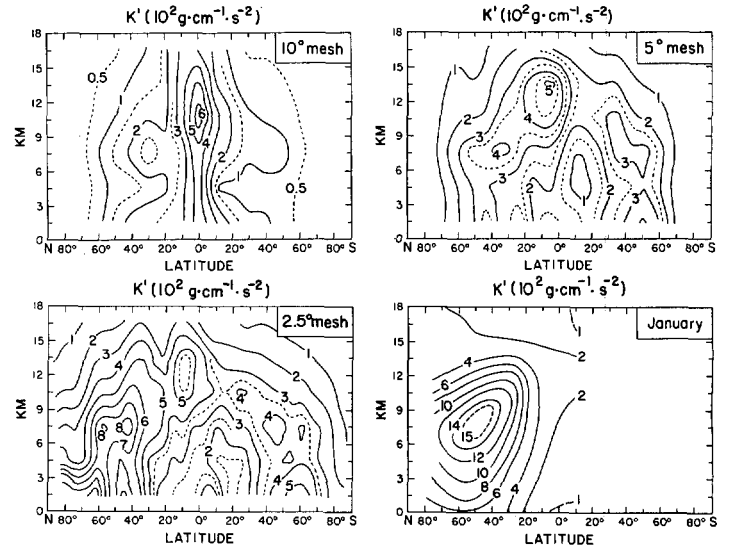


FIGURE 11.—Latitude-height distributions of the zonally averaged eddy kinetic energy defined by eq (4) for the three mesh cases. The lower right picture shows observed K' for January, after Oort and Rasmusson (1970).

where λ is the longitude. We also introduce the density-weighted mean, denoted by \hat{A} , which is defined by

$$\hat{A} = \overline{\rho A} / \bar{\rho},$$

$$A = \hat{A} + A',$$

and

$$\overline{\rho A'} = 0. \quad (2)$$

Applying the zonal average [eq (1)] to the definition of kinetic energy, we find that

$$\frac{1}{2} \overline{\rho(u^2 + v^2)} = \bar{K} + K'$$

where

$$\bar{K} = \frac{1}{2} \bar{\rho} (\hat{u}^2 + \hat{v}^2), \quad (3)$$

and

$$K' = \frac{1}{2} (\overline{\rho u'^2} + \overline{\rho v'^2}). \quad (4)$$

We call \bar{K} the zonal kinetic energy and K' the eddy kinetic energy.

Figures 10 and 11 show the latitude-height distributions of \bar{K} and K' , respectively, computed for the three cases. The differences in the patterns of \bar{K} for the three different horizontal resolutions are expected because the zonal component of wind is primarily influencing the zonal kinetic energy as is shown by figure 8. The differences in the patterns of K' , on the other hand, are very revealing. In the 10° mesh case, we notice the maximum of K' located at the Equator and very weak local maxima in the middle latitudes of both hemispheres. With improved

horizontal grid resolution, the intensity of the middle latitude maxima strengthens by a factor of almost two whereas the tropical maximum is gradually weakened. Manabe et al. (1970b) noted this same tendency toward an increase in the horizontal grid resolution improving the intensity of the eddy kinetic energy maximum in the middle latitudes. The location of the K' maximum in the Northern Hemisphere for the 2.5° horizontal mesh case is in agreement with the observed distribution by Oort and Rasmusson (1970), shown as the lower right picture in figure 11, although the intensity of the computed K' is still too small. Another discrepancy between the computed K' and the observed K' is the local maximum in the Tropics of the model. This local maximum of eddy kinetic energy in the Tropics seems attributable to excessive development of disturbances caused by moist convection in the intertropical convergence zones. We have recently rerun the 5° mesh case using a slightly larger value of nonlinear dissipation and found, even in the 5° mesh case, that the tropical maximum of K' can be greatly reduced.

Figure 12A shows the latitude-height distributions of meridional eddy angular momentum flux, $\overline{u'v'}$, computed from the three cases. Because the primed quantities are deviations from the density-weighted mean values, we should have shown $\overline{\rho u'v'}$, including the density. However, in order to provide an easier comparison with observed data, we omitted the density factor in this presentation. Figure 12B shows the *observed* distributions corresponding to the quantity, $\overline{u'v'}$. The left picture was drawn based on data by Kidson et al. (1969) for the tropical region. The sources of data for the right picture are Holopainen (1967) for the Northern Hemisphere and Obasi (1963) for the Southern Hemisphere. In Obasi's data there is some indication of a local minimum in the Tropics. The distribution by Kidson et al. (1969) clearly shows the presence of eddy momentum flux in the upper troposphere from the winter to the summer hemisphere, comparable in magnitude to the poleward fluxes in middle latitudes. Dickinson (1970) argues that these fluxes are the consequence of planetary wave sources in the Tropics of the summer hemisphere. The sources for these waves are very likely planetary-scale asymmetries caused by the release of latent heat in the equatorial trough zones. The computations from the three cases all simulate the southward eddy momentum transport crossing the Equator, although the computations give values a little too large when compared with the observed values.

Concerning the middle-latitude eddy momentum transports, the 10° mesh is not able to reproduce the proper intensities, and at least a 5° mesh is needed for a reasonable simulation of the eddy momentum transport. In fact, as far as the Northern Hemisphere is concerned, the distribution of $\overline{u'v'}$ with the 5° mesh agrees very well with a combined picture of two observed distributions shown in figure 12B. This may be the reason why the zonal wind distribution with the 5° mesh shown in figure 8 gives

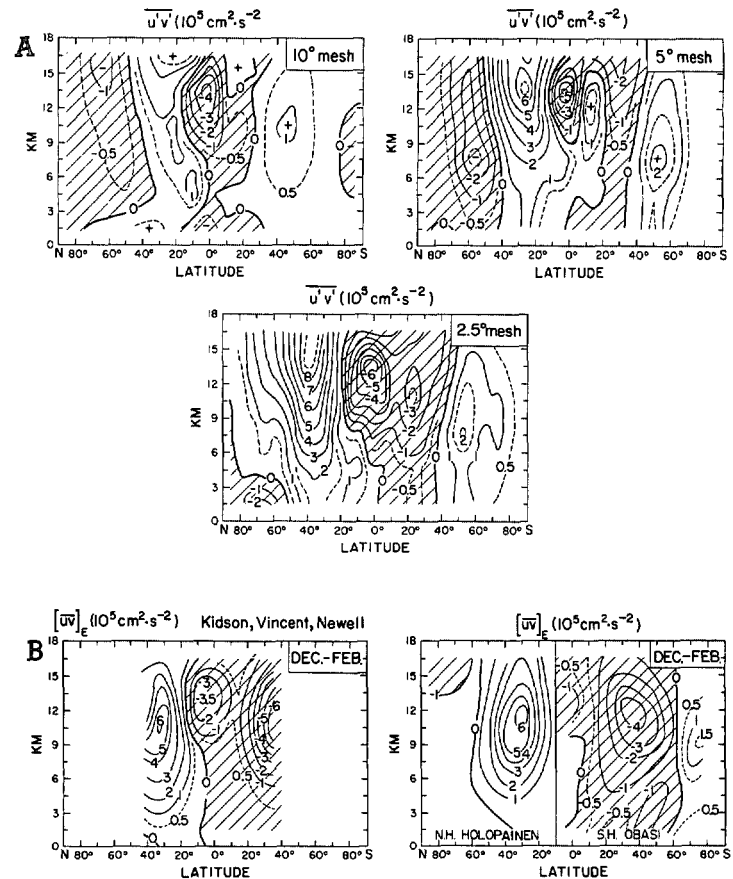


FIGURE 12.—(A) latitude-height distributions of meridional eddy angular momentum flux, $\overline{u'v'}$, for the three mesh cases; (B) latitude-height distributions of $\overline{u'v'}$ from observed data as indicated. Northward values are positive.

better agreement with the observed state in the Northern Hemisphere. Conversely, the shortcoming in simulation of the Southern Hemisphere westerly jet with the 5° mesh may be due to the mesh failure to obtain a proper distribution of $\overline{u'v'}$ in the Southern Hemisphere. The 2.5° mesh case shows an improvement in simulating the eddy momentum transport in the Southern Hemisphere which may give a better representation of the Southern Hemisphere westerly jet. However, the 2.5° mesh case gives a larger and more extensive northward eddy momentum transport in the Northern Hemisphere which may have caused the northward shift of the Northern Hemisphere jet shown in figure 8.

It is interesting to note that the large *southward* (negative values) eddy momentum transport in the Tropics (fig. 12A) is roughly compensated by the large *northward* (positive values) momentum transport by the mean circulation, \overline{uv} , as shown in figure 13. The observed distribution is after Kidson et al. (1969). As mentioned earlier in connection with the observed distribution of \overline{v} in figure 9, we should not trust the large negative values of \overline{uv} in the Northern Hemisphere because the observed values \overline{v} of in the middle latitudes of the Northern Hemi-

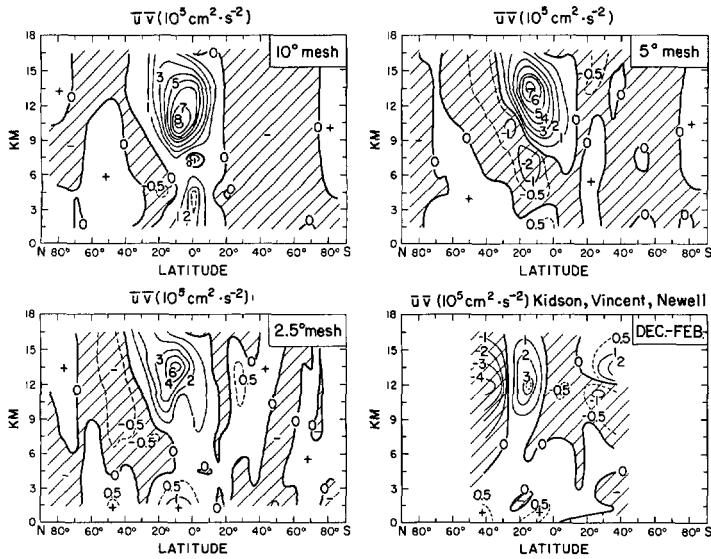


FIGURE 13.—Latitude-height distributions of meridional momentum transport by the mean circulation, $\bar{u}\bar{v}$, for the three mesh cases and from observed data. Northward values are positive.

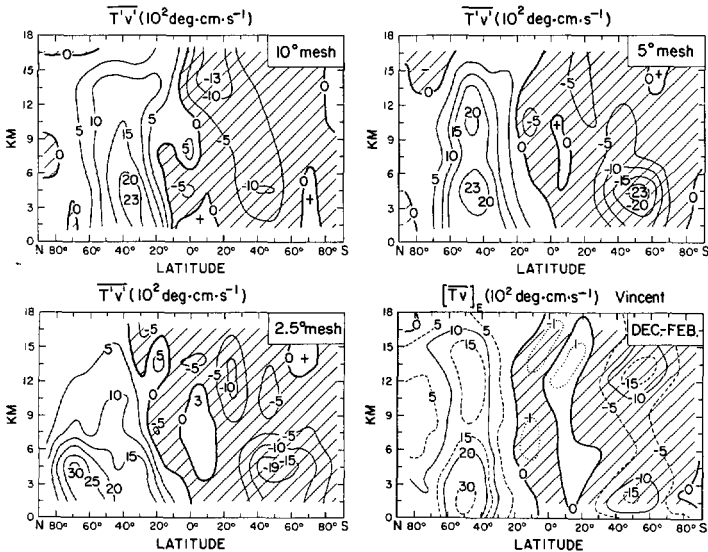


FIGURE 14.—Latitude-height distributions of meridional eddy heat transport, $\bar{T}'\bar{v}$, for the three mesh cases and from observed data. Northward values are positive.

sphere are not reasonable. Otherwise, the distribution of $\bar{u}\bar{v}$ from the 2.5° mesh seems to agree reasonably well with the observations.

Figure 14 shows the zonally averaged distributions of meridional eddy heat transports, $\bar{T}'\bar{v}$, computed from the three different cases. The observed distribution shown as the lower right picture is after Vincent (1969). It is interesting to note that the distributions of $\bar{T}'\bar{v}$ from the three different cases are similar. In fact, the distribution from the 5° mesh appears to agree well with the observed distribution. This was not the case in the distribution of $\bar{u}\bar{v}$,

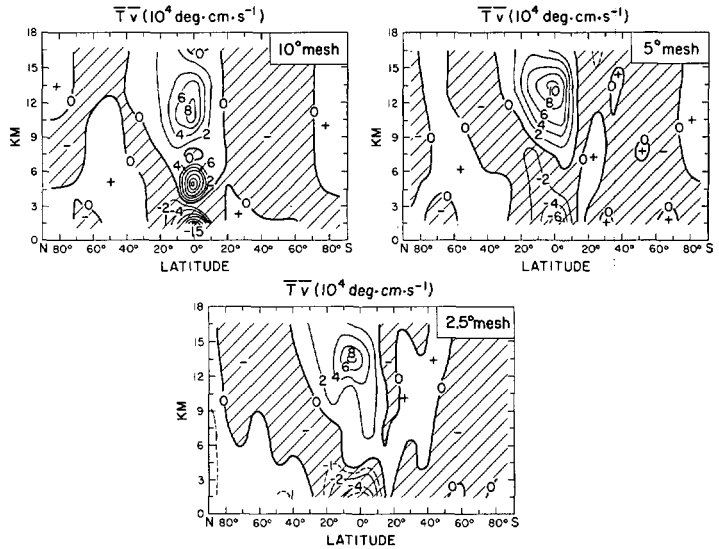


FIGURE 15.—Latitude-height distributions of meridional heat transport by the mean circulation, $\bar{T}\bar{v}$, for the three mesh cases. Northward values are positive.

that is more sensitive to differences in the horizontal grid resolution. Notice that large magnitudes of $\bar{T}'\bar{v}$ occur in the middle latitudes, but not in the Tropics. This is expected because the horizontal temperature gradient is weaker in the Tropics than in middle latitudes. The middle latitude maxima are obviously related to baroclinic waves.

Figure 15 shows the zonally averaged distributions of meridional heat transport by the mean circulation, $\bar{T}\bar{v}$. Although the magnitudes of $\bar{T}\bar{v}$ are very much larger than those of $\bar{T}'\bar{v}$ simply because the magnitude of \bar{T} is larger than T' , the main contribution to the time rate of change in the temperature is the horizontal divergence of $\bar{\rho}\bar{T}\bar{v}$, or more correctly speaking, $\bar{\rho}\hat{T}\bar{v}$. As noted in our previous study, Washington and Kasahara (1970), the horizontal divergence of $\bar{\rho}\hat{T}\bar{v}$ tends to balance the vertical divergence of $\bar{\rho}\hat{T}\hat{w}$. In any case, we see that increasing the horizontal grid resolution results in reducing heat transport by the mean circulation.

General conclusions drawn from studying figures 14 and 15 for heat transports are applicable to water vapor transports. Figures 16 and 17 show the distributions of eddy and mean circulation specific-humidity transport, $\bar{q}'\bar{v}$ and $\bar{q}\bar{v}$, respectively, computed from the three mesh cases. Figure 18 shows the distribution of $\bar{q}\bar{v}$ computed by Starr et al. (1969) based on 1 year's data. By comparing figure 18 with figures 16 and 17, keeping in mind that the observed distribution is annual rather than for December–February, we see that the poleward transports of water vapor in the middle latitudes of both hemispheres are primarily due to the eddy motions and that the equatorward transports in the Tropics are caused by the mean circulation. Also, the observed poleward eddy transports of water vapor are comparable in magnitude to those simulated in the 2.5°

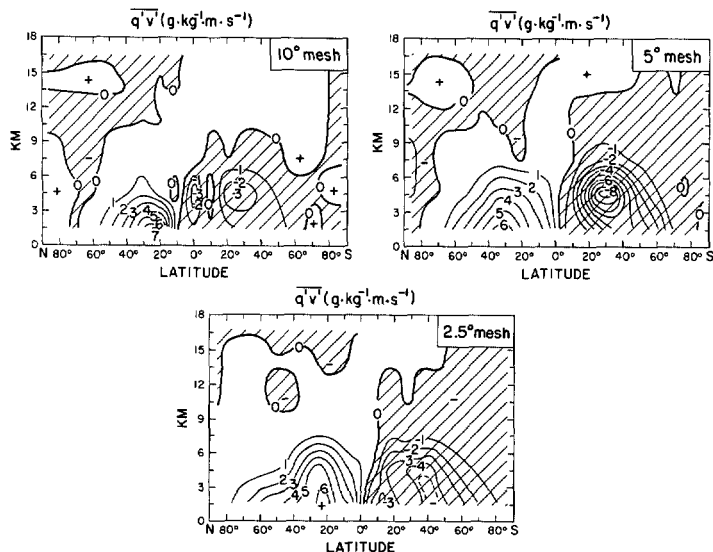


FIGURE 16.—Latitude-height distributions of eddy specific-humidity transport, $\overline{q'v'}$, for the three mesh cases. Northward values are positive.

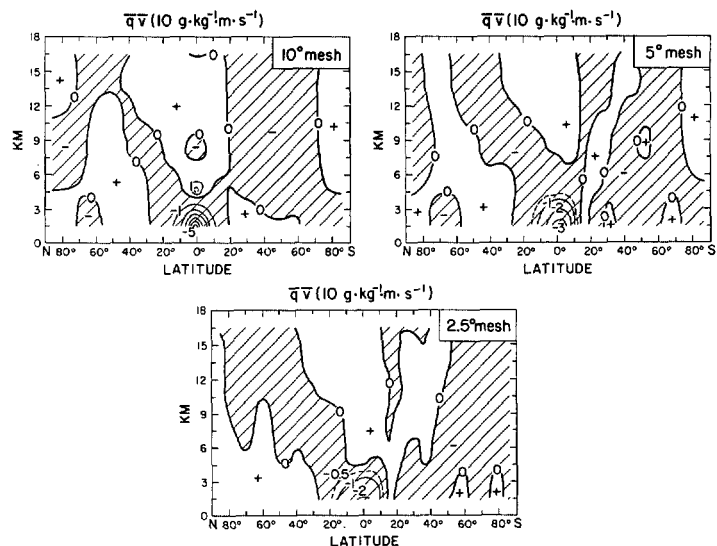


FIGURE 17.—Same as figure 16, but for mean circulation specific-humidity transport, \overline{qv} . Northward values are positive.

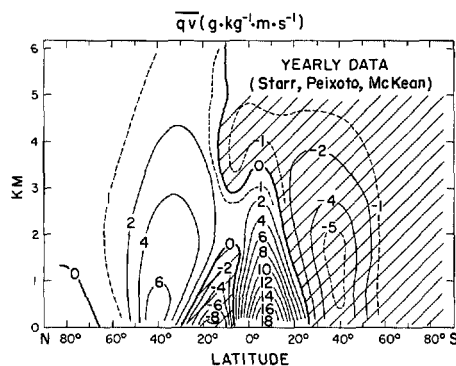


FIGURE 18.—Latitude-height distributions of total specific-humidity meridional transport, \overline{qv} , from *yearly* observed data. Northward values are positive.

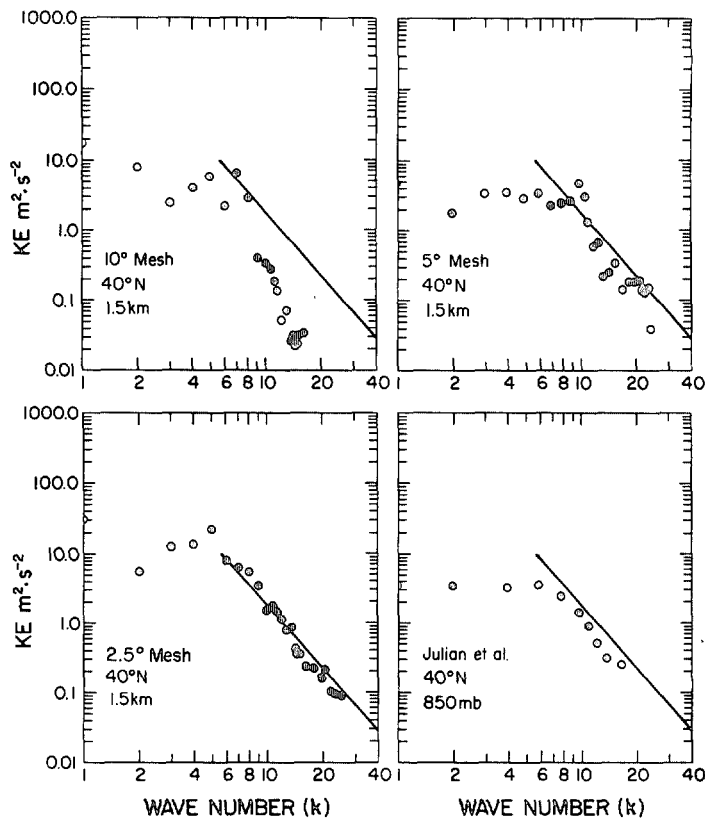


FIGURE 19.—Spectra of kinetic energy, KE , as a function of wave number k for the three mesh cases compared with observed data (lower right picture). The straight line shows a -3 power distribution as a reference.

mesh case. The 2.5° mesh case appears to produce smaller magnitude transports by the mean circulation than does the 5° mesh case.

5. SPECTRAL DISTRIBUTION OF KINETIC ENERGY

In order to further investigate the effects of increased horizontal grid resolution on eddy motions, we will study the spectral distributions of eddy kinetic energy at various latitudes and levels based on data from the three different grid versions.

Figure 19 shows the spectral distributions of eddy kinetic energy (per unit mass) as a function of longitudinal wave number k at 40° N and 1.5-km altitude. The upper left and right pictures are for the 10° and 5° meshes, and the lower left picture is for the 2.5° mesh. The values are averaged for the period of days 21–30. The lower right picture shows the observed distribution at 850 mb computed by Julian et al. (1970) using data from the National Meteorological Center. Note that their spectral distribution is computed for the kinetic energy of transient disturbances after removing the stationary component of the wind field. Therefore, the observed distribution underestimates the total eddy kinetic energy spectrum, particularly in the low wave number components. The slanted

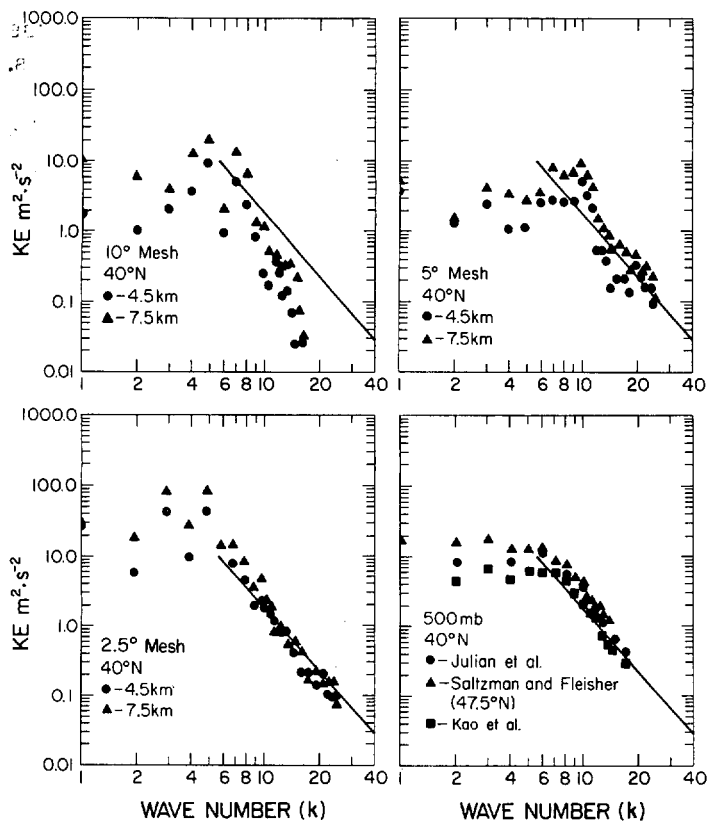


FIGURE 20.—Same as figure 19, except computed at different altitudes as indicated.

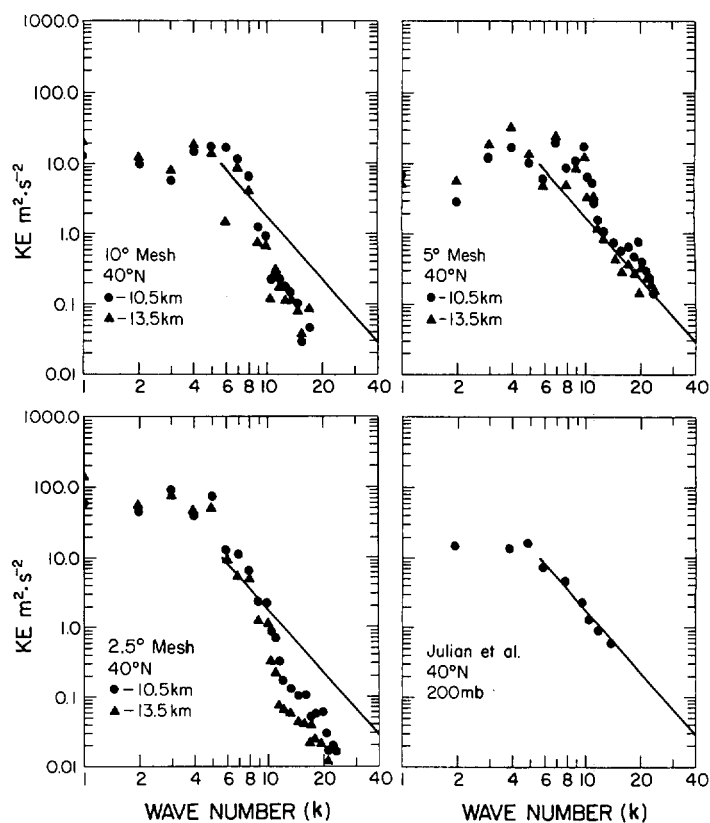


FIGURE 21.—Same as figure 19, except computed at different altitudes, as indicated.

straight line in each figure shows a k^{-3} distribution as a reference. For the 10° mesh case the spectral distribution in high wave number components has a steeper slope than a -3 spectrum, indicating that the resolution for high wave number components is insufficient. The generation of eddies in high wave number components is very much improved in the 5° mesh case. When the horizontal grid size is reduced further to 2.5° , the spectral intensity increases in the low wave number components.

Figures 20 and 21 show distributions at 40°N similar to figure 19, but at the 4.5- and 7.5-km levels and the 10.5- and 13.5-km levels, respectively. In figure 20 we have also included data from Saltzman and Fleisher (1962) and Kao et al. (1966) at 500 mb for comparison. The amount of kinetic energy in low wave number components increases with height as expected. As found in figure 19, the amount of kinetic energy in the higher wave number components increases as the horizontal resolution of the grid is increased from 10° to 5° , but further refinement of the grid to 2.5° increases the amount of kinetic energy in the lower wave number components. One exception is that the amount of kinetic energy in the upper troposphere for the high wave number components seen in figure 21 appears to show less magnitude in the 2.5° mesh case than in the 5° mesh case.

Figures 19 to 21 show the spectral distribution of kinetic energy (per unit mass) at 40°N but at various

heights. Figures 22, 20, and 23 show the spectra at 4.5- and 7.5-km levels, but for 30°N , 40°N , and 50°N , respectively. Differences at these latitudes are minor in comparison with the differences in height discussed in connection with figures 19 to 21. This fact is also in agreement with the observed spectra.

Consistent with our conclusions in section 4, we find that the 10° mesh generates small eddy activity in the high wave number components. This deficiency is corrected in the 5° mesh. A major difference between the 5° and 2.5° mesh cases is found in the increase of kinetic energy in the low wave number components 1 to 4. This conclusion is in agreement with the recent finding by Manabe et al. (1970b) in which they observed the increase of kinetic energy in low wave number components when the horizontal grid size is reduced from approximately 500 to 250 km in a hemispheric model.

It is well known that the large-scale motions of the atmosphere are approximately two-dimensional and non-divergent. Lilly (1969) studied the kinetic energy spectral distribution of the two-dimensional nondivergent flow produced by monochromatic random forcing present in a narrow spectral band at a wave number, say k_e . He found that a $k^{-5/3}$ spectrum develops in the wave number range $k < k_e$ (in long waves) and a k^{-3} distribution in the range $k > k_e$ (in short waves). This was predicted by Kraichnan (1967) and also discussed by Leith (1968). As pointed out

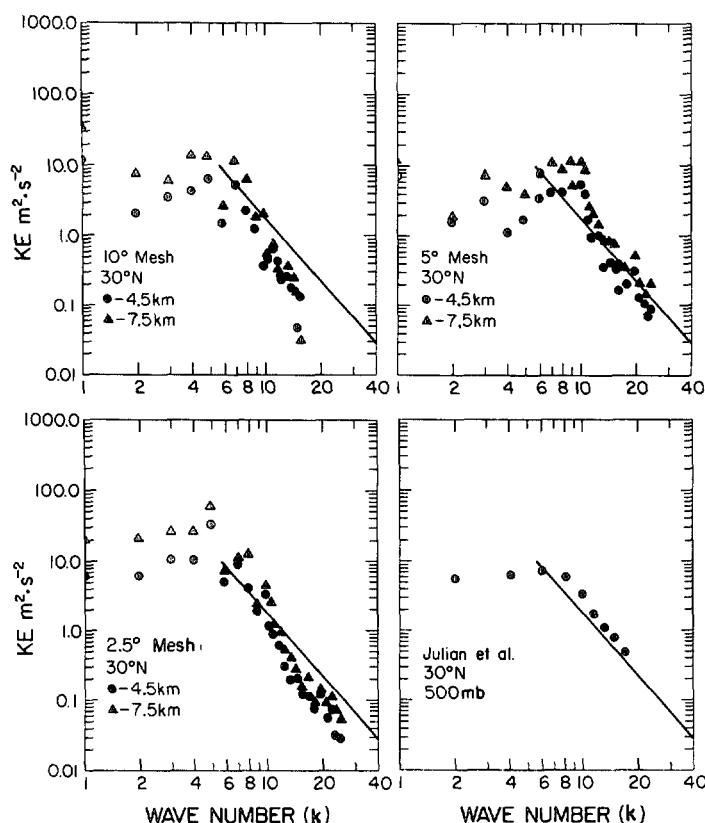


FIGURE 22.—Same as figure 19, except computed at different altitudes and a different latitude as indicated.

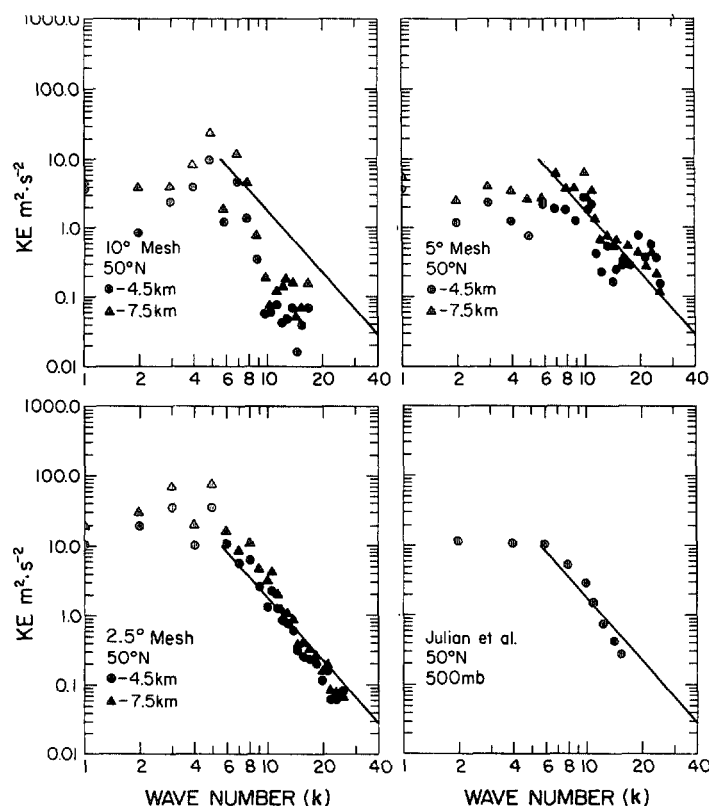


FIGURE 23.—Same as figure 19, except computed at different altitudes and a different latitude as indicated.

by Horn and Bryson (1963) and Wiin-Nielsen (1967), the kinetic energy spectrum may be grouped into two regimes, one in the lower wave number region and the other in the higher wave number region divided somewhere around a wave number between, say, 6 to 8. This feature can be seen in figures 19 to 23 in which the kinetic energy spectra in the wave number regime higher than wave numbers 6 to 8 are well represented by a k^{-3} distribution. A similar feature has been reported by Manabe et al. (1970a) in their model.

Since large-scale atmospheric motions are quasi two-dimensional and nondivergent, we may be able to interpret the present result in light of two-dimensional turbulence theory in the following way. The eddy kinetic energy in the middle latitudes owes its major energy source to the disturbances of wave numbers, say, 6 to 8, created by baroclinic instability. The input energy is then cascading toward longer waves and vorticity is cascading toward shorter waves. The mesh with higher horizontal grid resolution is capable of resolving baroclinic waves more accurately and produces less energy dissipation (due to nonlinear viscosity) at the wave numbers of maximum baroclinic instability. Thus, more energy can be transported to the longer waves and this may account for a significant increase in the amount of kinetic energy in the long wave regime of wave numbers 1 to 4 for the 2.5° mesh case.

6. CONCLUSIONS

In this paper the effect of varying the horizontal grid resolution in the NCAR GCM was investigated in conjunction with the simulation of January climate. For the same vertical resolution of six layers with 3-km thickness, time integrations were made with three different horizontal grid resolutions of 10°, 5°, and 2.5° in both longitude and latitude. Conclusions drawn from this comparative study follow.

1. The 10° mesh is too coarse. Meridional transports of momentum, heat, and water vapor are done mostly by the mean circulation. The intensity of eddy motions in the middle latitudes is very much undervalued and that in the Tropics is exaggerated.

2. The 5° mesh is acceptable for the study of climate simulation. However, the intensity of eddy motions in the middle latitudes is still somewhat underestimated. As in the 10° mesh case, a maximum of eddy kinetic energy appears in the Tropics, but its intensity can be controlled. The effect of the mean circulation in the meridional transports of momentum, heat, and water vapor still appears to be overestimated in the Tropics.

3. The 2.5° mesh significantly improves the intensity of eddy motions in the middle latitudes as compared with the 5° mesh. The meridional transports of momentum, heat, and water vapor by the mean circulation in the 2.5° mesh case are reduced and are closer to the observed values. Therefore, it is desirable to use the 2.5° mesh rather than the 5° mesh even for climate simulation. One obstacle to the use of the 2.5° mesh is in the computer time required; it takes 8 hr to run 1 atmospheric day on NCAR's Control Data Corporation 6600 computer.

ACKNOWLEDGMENTS

The authors express their gratitude to many members of the NCAR Computing Facility who assisted in the efficient operation of the Control Data Corporation 6600 computer to carry out this experiment. P. Julian and J. L. Holloway, Jr. have offered the authors useful comments on the manuscript. Thanks are also due Ann Lundberg for assistance in the preparation of this manuscript.

REFERENCES

- Crutcher, Harold L., "Meridional Cross-Sections Upper Winds Over the Northern Hemisphere," *Technical Paper No. 41*, U.S. Weather Bureau, Washington, D.C., June 1961, 307 pp.
- Dickinson, Robert E., "Cross-Equatorial Eddy Momentum Fluxes as Evidence of Tropical Planetary Wave Sources," *NCAR Manuscript No. 70-8*, National Center for Atmospheric Research, Boulder, Colo., 1970, 11 pp.
- Holopainen, E.O., "On the Mean Meridional Circulation and the Flux of Angular Momentum Over the Northern Hemisphere," *Tellus*, Vol. 19, No. 1, Stockholm, Sweden, 1967, pp. 1-13.
- Horn, Lyle H., and Bryson, Reid A., "An Analysis of the Geostrophic Kinetic Energy Spectrum of Large-Scale Atmospheric Turbulence," *Journal of Geophysical Research*, Vol. 68, No. 4, Feb. 15, 1963, pp. 1059-1064.
- Julian, Paul R., Washington, Warren M., Hembree, L., and Ridley, C., "On the Spectral Distribution of Large-Scale Atmospheric Kinetic Energy," *Journal of the Atmospheric Sciences*, Vol. 27, No. 3, May 1970, pp. 376-387.
- Kao, S.-K., Wendell, L. L., and Noteboom, D. A., "Longitude-Time Power- and Cross-Spectra of Atmospheric Quantities," *Atmospheric Turbulence and Transport Research Paper No. 10*, University of Utah, Salt Lake City, 1966, 240 pp.
- Kasahara, Akira, "Computer Simulation of the Earth's Atmosphere," *Proceedings of the Section on Numerical Methods in Gasdynamics of the Second International Colloquium on Gasdynamics of Explosion and Reacting Systems, Novosibirsk, U.S.S.R., August 19-23, 1969*, NCAR Manuscript No. 70-22, National Center for Atmospheric Research, Boulder, Colo., 1970, 16 pp.
- Kasahara, Akira, and Washington, Warren M., "NCAR Global General Circulation Model of the Atmosphere," *Monthly Weather Review*, Vol. 95, No. 7, July 1967, pp. 389-402.
- Kasahara, Akira, and Washington, Warren M., "Thermal and Dynamical Effects of Orography on the General Circulation of the Atmosphere," *Proceedings of the WMO/IUGG Symposium on Numerical Weather Prediction, Tokyo, Japan, November 26-December 4, 1968*, Meteorological Society of Japan, Tokyo, Mar. 1969, pp. IV-47-IV-56.
- Kidson, John W., Vincent, Dayton G., and Newell, Reginald E., "Observational Studies of the General Circulation of the Tropics: Long Term Mean Values," *Quarterly Journal of the Royal Meteorological Society*, Vol. 95, No. 404, London, England, Apr. 1969, pp. 258-287.
- Kraichnan, Robert H., "Inertial Ranges in Two-Dimensional Turbulence," *The Physics of Fluids*, Vol. 10, No. 7, July 1967, pp. 1417-1423.
- Leith, Cecil E., "Diffusion Approximation for Two-Dimensional Turbulence," *The Physics of Fluids*, Vol. 11, No. 3, Mar. 1968, pp. 671-672.
- Lilly, Douglas K., "Numerical Simulation of Two-Dimensional Turbulence," *The Physics of Fluids, Supplement II: High-Speed Computing in Fluid Dynamics*, Vol. 12, No. 12, Dec. 1969, pp. II-240-II-249.
- Manabe, Syukuro, Holloway, J. Leith, Jr., and Stone, Hugh M., "Tropical Circulation in a Time-Integration of a Global Model of the Atmosphere," *Journal of the Atmospheric Sciences*, Vol. 27, No. 4, July 1970a, pp. 580-613.
- Manabe, Syukuro, Smagorinsky, Joseph, Holloway, J. Leith, Jr., and Stone, Hugh M., "Simulated Climatology of a General Circulation Model With a Hydrologic Cycle: III. Effects of Increased Horizontal Computational Resolution," *Monthly Weather Review*, Vol. 98, No. 3, Mar. 1970b, pp. 175-212.
- Obasi, G. O. P., "Poleward Flux of Atmospheric Angular Momentum in the Southern Hemisphere," *Journal of the Atmospheric Sciences*, Vol. 20, No. 6, Nov. 1963, pp. 516-528.
- Olinger, J., Welck, Robert R., Kasahara, Akira, and Washington, Warren M., *Description of NCAR Global Circulation Model*, National Center for Atmospheric Research, Boulder, Colo., 1970, 94 pp.
- Oort, Abraham H., and Rasmusson, Eugene M., "Atmospheric Circulation Statistics—A Compilation of Zonally Averaged, Monthly, and Seasonal Statistics of the Atmospheric Circulation North of 10°S Based on a 5-Year Sample," *Geophysical Fluid Dynamics Laboratory, NOAA, Princeton, N.J., 1970*, (unpublished manuscript).
- Palmén, Erik H., "General Circulation of the Tropics: A Survey Paper," *Proceedings of the Symposium on Tropical Meteorology, Rotorua, New Zealand, November 5-13, 1963*, New Zealand Meteorological Service, Wellington, 1964, pp. 3-30.
- Palmén, Erik H., and Newton, C. W., *Atmospheric Circulation Systems*, Academic Press, Inc., New York, N.Y., 1969, 603 pp.
- Peixoto, José P., and Crisi, A. R., "Hemispheric Humidity Conditions During the IGY," *Planetary Circulation Project, Scientific Report No. 6*, Contract No. AF19(628)-2408, Massachusetts Institute of Technology, Cambridge, Nov. 1965, 166 pp.
- Saltzman, Barry, and Fleisher, Aaron, "Spectral Statistics of the Wind at 500 Mb," *Journal of the Atmospheric Sciences*, Vol. 19, No. 2, Mar. 1962, pp. 195-204.
- Smagorinsky, Joseph, "General Circulation Experiments With the Primitive Equations: I. The Basic Experiment," *Monthly Weather Review*, Vol. 91, No. 3, Mar. 1963, pp. 99-164.
- Starr, Victor P., Peixoto, José P., and McKean, R. G., "Pole-to-Pole Moisture Conditions," *Pure and Applied Geophysics*, Vol. 73, No. 2, Basel, Switzerland, 1969, pp. 85-116.
- Taljaard, J. J., van Loon, Harry, Crutcher, Harold L., and Jenne, Roy L., *Climate of the Upper Air: Part 1. Southern Hemisphere, Volume 1. Temperatures, Dew Points, and Heights at Selected Pressure Levels*, NAVAIR 50-1C-55, U.S. Naval Weather Service, Washington, D.C., Sept. 1969, 6 pp. plus 134 figures.
- van Loon, Harry, Taljaard, J. J., Jenne, R. L., and Crutcher, Harold L., *Climate of the Upper Air: Part 1. Southern Hemisphere, Volume 2. Zonal and Meridional Geostrophic Wind Components*, NAVAIR 50-1C-56, U.S. Naval Weather Service, Washington, D.C., 1971, 11 pp., 18 figs., 144 charts.
- Vincent, Dayton G., "Seasonal Changes in the Global Atmospheric Energy Balance and Results for Restricted Regions," Ph. D. thesis, Department of Meteorology, Massachusetts Institute of Technology, Cambridge, Nov. 1969, 174 pp.
- Washington, Warren M., and Kasahara, Akira, "A January Simulation Experiment With the Two-Layer Version of the NCAR Global Circulation Model," *Monthly Weather Review*, Vol. 98, No. 8, Aug. 1970, pp. 559-580.
- Wiin-Nielsen, A., "On the Annual Variation and Spectral Distribution of Atmospheric Energy," *Tellus*, Vol. 19, No. 4, Stockholm, Sweden, Nov. 1967, pp. 540-559.

[Received July 27, 1970; revised October 30, 1970]

PICTURE OF THE MONTH

Smoke From Slash Burning Operations

FRANCES C. PARMENTER

Applications Group, National Environmental Satellite Service, NOAA, Suitland, Md.

Agricultural burning to clear land or to dispose of crop residue or slash is practiced throughout the world. This year, a large area of smoke, emanating from slash burning operations in Central America, was observed on Applications Technology Satellite 3 (ATS 3) photographs. The smoke was clearly visible for a 25-day period beginning Apr. 18, 1971. S. Bonis, of Guatemala, indicated (Bonis 1970) that that country's annual slash-burn program usually begins in February and lasts until the onset of the rainy season in May.

Smoke appears to originate from two areas: Tabasco, Mexico and the lowlands along the Gulf of Honduras. During the first 12 days, this area was generally located in the southwest quadrant of a surface High. The resulting southerly flow carried the smoke from Mexico northward across the Gulf of Mexico and, on some days, as far north as New Orleans, La. During the late afternoon and early evening, local onshore winds often carried the smoke back over land, toward the mountain barriers.

On the first day, April 18, the smoke was only faintly visible. By the next day (fig. 1A), the smoke was more dense and extended well offshore (S). On April 22 (fig. 1B), smoke covers a large area of the lowlands just north of the Sierra Madre Range (S) and extends northward to the front (T). Another area of smoke can also be seen north of Honduras (U). (The smoke pattern over the Gulf of Honduras undergoes little day-to-day variation during this period.)

During the next three days, anticyclonic flow continued to carry smoke northward and eastward in advance of the front. Smoke was reported as far east as Tampa, Fla., by April 24, and smoke and fog continued to be observed over the Florida peninsula as the front moved southward.

On April 26, another frontal system moved into the Gulf States and subsequently moved eastward, offshore. Once again an anticyclonic circulation dominated the Gulf of Mexico. The southerly flow over the burning area

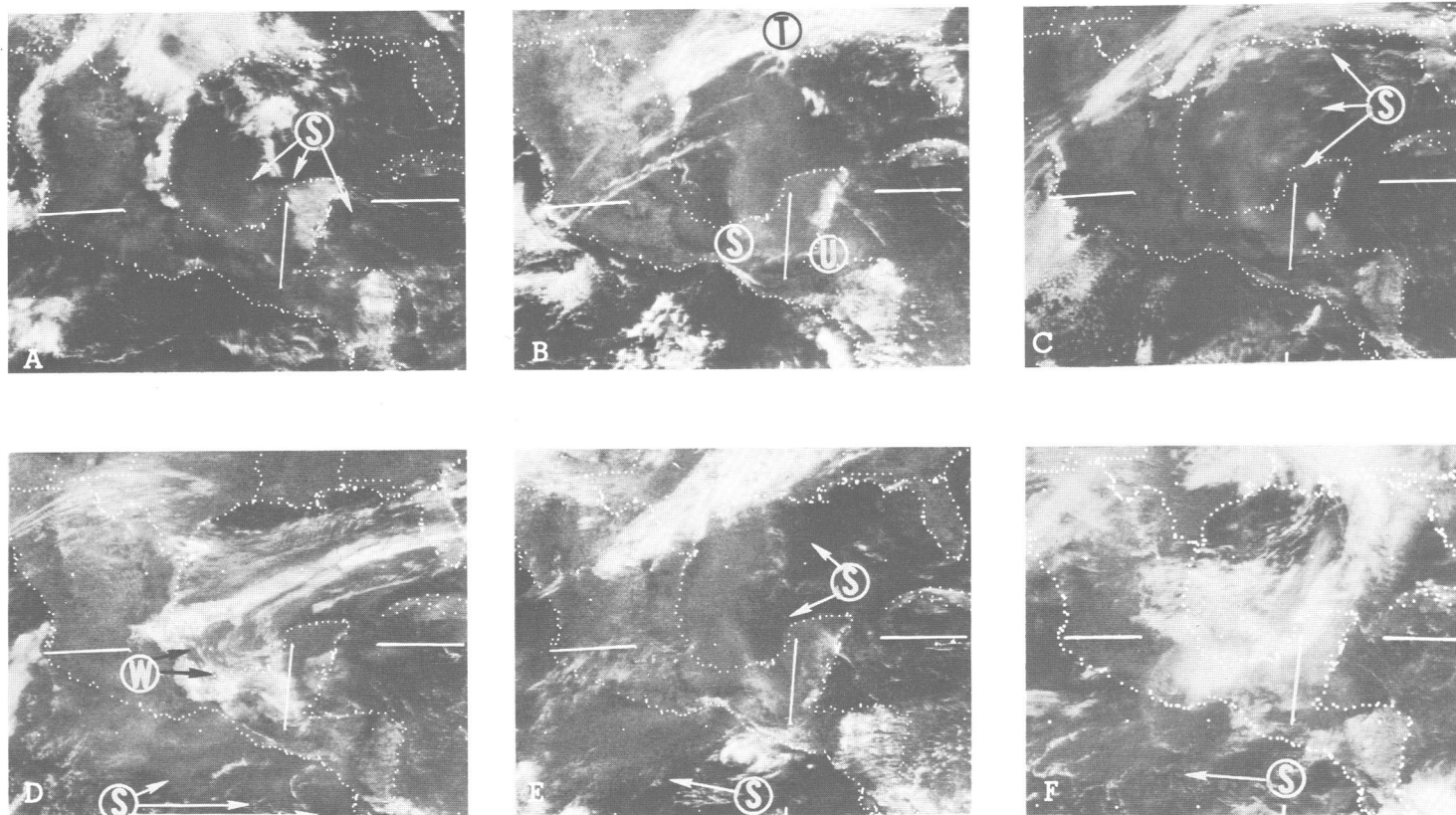


FIGURE 1.—ATS 3 observations of smoke from slash burning operations in Central America, 1971; (A) Apr. 19, 1527 GMT, (B) Apr. 22 1718 GMT, (C) Apr. 29, 1523 GMT, (D) May 1, 1623 GMT, (E) May 6, 1641 GMT, and (F) May 12, 1510 GMT.

gradually increased and by April 29 smoke once again covered the western half of the Gulf (S, fig. 1C).

A strong frontal system moved into the Gulf of Mexico on May 1. With the change in low-level flow, fog and stratus covered the coastal lowlands (W, fig. 1D), and airborne smoke moved southward across Southern Mexico and out over the Pacific Ocean (S, fig. 1D). On May 4, smoke covered an area between 10° and 15°N and 90° and 108°W. A subsequent change in low-level flow on May 5 once again allowed the smoke to drift northward across the Gulf of Mexico while it gradually diminished over the Pacific (S, fig. 1E).

A large frontal system brought light to moderate rain to this area on May 12 (fig. 1F), thus ending the burning season in Central America. Even at this time some smoke (S) could still be seen over the Pacific.

The effect of this annual burning on the weather of the southeastern United States is, presently, not clearly understood. Barrett et al. (1970) state that small solid particles can affect the climate of an area by serving as cloud nuclei and by altering the radiation budget. They note that an increase in cloud condensation nuclei over the tropical oceans leads to greater cloud stability and reduced rainfall; on the other hand, an increase in ice-nucleating particles would tend to increase precipitation in middle

and high latitudes. They also suggest that droplet growth may be partially inhibited and cloud stability increased when organic matter is present on the surface of droplets. Holle (1969), in his study of the Florida drought, notes several cases in which an increase in nuclei has resulted in a decrease in precipitation.

Satellite photographs can provide valuable information on the areal extent of particulate matter from dust and sand storms as well as smoke from large fires. Further study which combines satellite data with other pertinent data may lead to a better understanding of some of the large seasonal variations in precipitation.

REFERENCES

- Barrett, E. W., Pueschel, R. F., Weickmann, Helmut K., and Kuhn, Peter M., "Inadvertent Modification of Weather and Climate by Atmospheric Pollutants," *ESSA Technical Report ERL 185-APCL 15*, Atmospheric Physics and Chemistry Laboratory, Boulder, Colo., Sept. 1970, 103 pp.
- Bonis, S., Instituto Geografico Nacional, Guatemala City, Guatemala, May 1971 (personal communication).
- Holle, Ronald L., "The Effect on Rainfall of Cloud Condensation Nuclei From Vegetation Fires Over South Florida During Spring Droughts," *ESSA Technical Memorandum ERLTM-AOML 4*, Atlantic Oceanographic and Meteorological Laboratory, Miami, Fla., Oct. 1969, 52 pp.